PHOTOMETRIC PARALLAXES AND SUBDWARF IDENTIFICATION FOR M-TYPE STARS

A THESIS

SUBMITTED TO THE GRADUATE SCHOOL

IN PARTIAL FULFILLMENT OF THE REQUIREMENTS

FOR THE DEGREE

MASTER OF SCIENCE

BY

DAYNA L. THOMPSON

ADVISOR: DR. THOMAS ROBERTSON

BALL STATE UNIVERSITY

MUNCIE, INDIANA

JULY 2012

Acknowledgements

First and foremost, I would like to thank my advisor, Dr. Thomas Robertson, for his endless guidance and patience throughout this project. I would also like to thank the Physics and Astronomy faculty and students, my family and friends, and everyone who put in observing time for this research.

Abstract

Photometric data on the Kron-Cousins photometric system have been obtained for 118 new late K to middle M-type stars with known distances. These data have been used to obtain absolute red magnitudes, to construct a color-magnitude diagram, and to compute a polynomial function for disk dwarf stars in the color range $1.5 \leq R\text{-}I < 2.0$, which can be used to compute absolute red magnitudes to be used for photometric parallaxes. Such photometric parallaxes allow new stellar distance estimations that are essential when modeling the spatial distribution of stars in our Galaxy. This is especially important for M-type stars, as they make up more than half of the mass of the Milky Way. Intermediate-band CaH observations have also been obtained in an ongoing effort to distinguish stellar luminosity classes and populations; R-L and R-I colors are used to identify possible subdwarf stars. A total of seven possible new subdwarfs and three previously known subdwarfs have been identified with this method.

Table of Contents

List of Tables

List of Figures

1. Introduction

1.1 Red Dwarf Stars

If you open an astronomy textbook to learn about red dwarf stars, you may be surprised that there is little, or in some cases, no information. This might give one the impression that these M-type stars are insignificant; however, they make up more than half of the stellar mass of our galaxy. In fact, they make up four fifths of the stellar population. Yet, detecting M dwarf stars and finding their place in the Milky Way galaxy is a difficult task (Farris et al. 2012).

These red dwarf stars that are no bigger than 0.6 solar masses go undetected due to their low luminosity. It is important to note that essentially all light produced in our galaxy comes from high luminosity stars, although they are few in number. Their domination in astronomical catalogs reflects this fact. Although early-type red dwarfs (K7 to M3) can be sampled out to 2-3 kpc, late-type red dwarfs (M4 to M9) are limited to samples within 100 pc. However, complete samples for late dwarf stars are available only out to 25 pc (Reid et al. 1995). To add a bit of perspective to these distances, consider that the diameter of our galactic plane is roughly 30 kpc.

It is because of their large numbers that M-type stars reflect the galactic structure of our Milky Way. In addition, their long lifespan affords data concerning their formation

and evolution. These are vital pieces for putting together the galactic puzzle (Spengler et al. 2012). The ability to determine distances to these stars will aid in defining their spatial distribution within our galaxy.

1.2 Parallax Methods

Determining the distances to stars is a difficult and time consuming process regardless of the technique used. Astronomers can measure distances to nearby stars using their annual periodic apparent displacement, a technique called trigonometric parallax. Using the star's change of location in the night sky in comparison to distant background stars, a parallax angle (measured in arcseconds) is found. Since both the Sun and target star are moving in the Milky Way, their relative positions to one another change with time. As a result, one requires observations over a few years to solve for these so-called proper motions. Once the parallax angle is known, basic trigonometry can be applied such that the following relation for distance is obtained

$$d(pc) = \frac{1}{p(")} \qquad 1.1$$

where *p(")* is the parallax in arcseconds and *d(pc)* is the distance to the star in parsecs. Trigonometric parallax can be used for stars out to distances of ~200 pc. This study uses stars out to ~50 pc, averaging a distance of ~20 pc.

Using the apparent magnitude of a star (how bright the star appears above Earth's atmosphere) and distance, one can calculate the absolute magnitude (the apparent brightness of the star seen from 10 pc) with the equation:

$$M_x = m_x - 5log_{10}\left(\frac{d}{10pc}\right) \quad 1.2$$

where M_x is the absolute magnitude and m_x is the apparent magnitude in any pass-band x. The magnitude scale is such that a difference of 5 magnitudes is a factor of 100 in brightness and brightness increases with decreasing magnitude. Using the apparent magnitude, astronomers usually use a magnitude of a short wavelength pass-band minus a longer one (for example, red minus infrared), giving a value known as color index. With many observations the absolute magnitude and color index of each star can be found. With these quantities, a color-magnitude diagram (CMD) can be plotted. Disk dwarfs in our Milky Way all follow a general trend on the CMD known as the disk main sequence. This trend allows one to determine photometric parallaxes, the ability to infer distance using the color and apparent magnitude of a star (Reid & Hawley 2005).

For stars that do not have an associated trigonometric parallax value, one can use these photometric parallaxes to estimate their distance. Advances have been made in the detection of M dwarf stars over the last two decades giving more complete CMDs and therefore more accurate photometric parallaxes. Siegel et al. (2002) use trigonometric parallax distance estimations from the *Hipparcos* catalog and photometry from Bessell (1990) and Leggett (1992) for faint dwarf stars. From these, distances can be found using their (M_R, (R-I)) CMD for late K to mid M-type disk dwarf stars ($0.4 \leq$ R-I < 1.5).

The *Hipparcos* survey, however, was limited by apparent magnitude and therefore the range of Siegel's work was limited to $M_R \sim 12$. The 4th Edition Yale

Trigonometric Parallax catalog (van Altena et al. 1995, hereafter YTP) targets stars that are in many cases selected from proper motion catalogs. Trigonometric parallax values from YTP allow Siegel's CMD to be expanded to include later M-type stars. This work offers photometric parallaxes for late M-type stars using these distances and photometry obtained remotely with the 0.9 m SARA telescope.

1.3 Subdwarf Population

Subdwarf stars are found in the stellar halo and throughout the thick disk of the Milky Way galaxy. The main difference between subdwarfs and disk dwarf stars is that subdwarfs are made up of fewer metals (in astronomy any element heavier than Hydrogen and Helium are metals). A star's metal abundance compared to that of the Sun's is known as its metallicity. Hence, a star with low metallicity has few metals than the Sun.

A star's metallicity is an indicator of its age. Since metals are made within stars, the amount of metals in our galaxy increases with time. Hence, a star with low metallicity is an older star, generally present at the formation of the Milky Way. Stars that are formed at different times in the galaxy have different systematic motions. Low metallicity subdwarfs, the oldest stars in the galaxy, also have higher systematic velocities and proper motions than disk dwarf stars. This makes them key targets for the proper-motion surveys that make up the YTP targets. Although approximately 99.7% of stars in the Milky Way make up the disk main sequence, statistically there will be more subdwarfs in the sample (Reid & Hawley 2005).

As a result of their low metallicity, subdwarfs have different spectroscopic features and therefore appear hotter at a given absolute magnitude than disk dwarf stars. Therefore, subdwarfs appear just below the disk main sequence on a (M_R, (R-I)) CMD. Their close proximity to the disk main sequence makes it difficult to detect these stars solely with the use of a CMD.

When observing a late-type star with no known distance, it is unclear whether it is a subdwarf, dwarf, or giant star. Therefore, it is important to find another technique to discern these stars. Figure 1 shows the separation of warm standard stars, red disk dwarfs, and red giant stars in what is called a color-color plot, or a two-color diagram (TCD). Three apparent magnitudes are used to construct this plot: red (R), infrared (I), and our Calcium Hydride (CaH) filter (L). The characteristics for these pass-bands, as well as for the visual (V) filter are listed in Table 1 below where $\Delta\lambda$ is the portion of the frequency spectrum that is transmitted and λ_{eff} is the effective wavelength for each filter. Warm standard stars, or warm disk dwarfs have higher temperatures than the other two sequences, therefore, appearing on the left hand side. These are stars that have temperatures too high to form molecules in their atmospheres. As a result, their upward trend in this plot is what one should see for a typical blackbody.

TABLE 1
Pass-band Characteristics

Band	$\Delta\lambda$ μm	λ_{eff} μm	Reference
V	0.50-0.59	0.542	Bessell (1979, 1990)
R	0.565-0.725	0.638	Bessell (1979, 1990)
I	0.73-0.88	0.787	Bessell (1979, 1990)
L	0.013	0.683	Robertson & Furiak (1995)

As temperature decreases, collisions between atoms in the atmosphere of stars become less violent, allowing molecules such as CaH to form. The effects of the formation of CaH can be seen at R-I ~ 0.7 in Figure 1, where cool dwarfs and red giants start to follow their own separate trends. The reason behind the red giants placement above the cool dwarfs on this plot can be explained while describing the differences between the two M-type stars. As hydrogen fusion ceases, dwarf stars (similar to our Sun) cool and increase in size becoming red giant stars. Their mass stays relatively the same while their radius increases, thus they have lower gravity than before. As a result, pressure in their atmosphere decreases and CaH molecules dissociate. Therefore, weaker CaH absorption is seen compared to disk dwarf stars at the same temperature, as they are smaller and have higher pressure atmospheres. This weak CaH absorption results in a lower L magnitude, or an increase in R-L, causing their placement in Figure 1. One is able to distinguish between red giant stars and disk dwarf stars when plotting ((R-L), (R-I)).

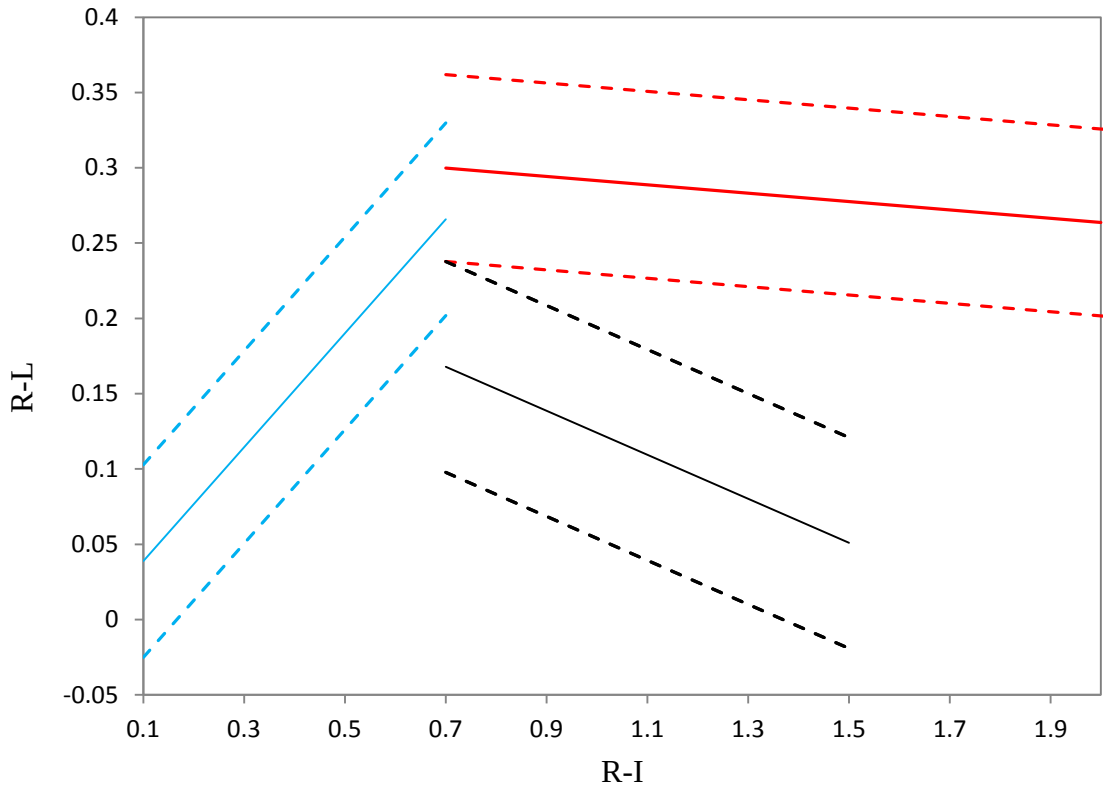

Fig. 1.- Two-Color Diagram for Warm Stars and Cool Dwarfs and Red Giants - Warm standard stars are plotted in blue, the disk M-dwarf sequence is in black, and red giants are in red. Dashed lines for each sequence are located at ±2σ in R-L from trends (Humphrey & Robertson 2008).

This ((R-L), (R-I)) TCD may prove useful when identifying subdwarf stars. Subdwarfs have previously been identified spectroscopically by comparing titanium oxide (TiO) band strengths to those of metal hydride bands (CaH in M subdwarfs) as described by Gizis (1997). As metallicity decreases in a star, TiO absorption decreases with but calcium hydride (CaH) is largely unaffected. These effects should be seen in a ((R-L), (R-I)) plot, separating subdwarf stars from cool disk dwarf stars as reduced TiO absorption affects (R-I) making the star appear at a higher temperature. Therefore, one

should see subdwarfs appear below the cool disk dwarf stars in Figure 1. This is also why these stars appear below the disk main sequence in a (M_R, (R-I)) CMD. If one can indeed identify subdwarf stars with this method, only three filters will be used thus reducing observation time.

Subdwarf identification for late K to late M-type stars has been researched in new studies by Jao et al. (2008). The paper stresses that a disk dwarf star with higher gravity appears nearby, or in some cases within the subdwarf region in plots defined by Gizis (1997), even if that star has a metal abundance similar to a disk dwarf star's. Although plotting ((R-L), (R-I)) should see this as well, it will be explained later how this TCD incorporates a star's placement on the (M_R, (R-I)) CMD. A similar technique was done by Jao et al. (2008) and aids in the correct identification subdwarf stars and subsequently their removal from the disk main sequence.

1.4 Applications of Photometric Parallax and Subdwarf Identification

In the attempt to describe the Milky Way's galactic structure, one uses photometric parallaxes to determine the distribution of stars that lie in a defined range of brightness. This is known as the luminosity function, as it defines the number of stars per unit absolute magnitude per unit volume. Therefore, the luminosity function can vary for different locations. There are different populations of stars that are defined by their location in the Milky Way (and as a result other characteristics dependent on location). There are models that incorporate this fact; however, alternative studies group stars by similarities such as luminosity, and not population. To help break the stars into groups of

similar traits, subdwarfs need to first be identified. This work presents a means to do so, as explained above.

Ideally, large samples of stars with known distances will adequately define stellar luminosity functions. However, due to the lack of identified dwarf stars, the luminosity function is not well defined for late M-type stars. Once a well-defined luminosity function exists, parameters that cannot be measured directly can now be attained. For instance, the initial mass function (IMF) is found using the luminosity function through a mass-luminosity relation. The IMF describes the distribution of stellar masses in a newly formed population (De Boer & Seggewiss 2008). Star formation theories have predicted the general shape of the IMF, making it a useful tool for astronomers studying star formation.

New luminosity and mass functions are presented by Bochanski et al. (2010) derived from the Sloan Digital Sky Survey (York et al. 2000) Data Release 6 photometry and the Two Micron All Sky Survey (Skrutskie et al. 2006). Their research utilizes the largest set of photometric observations to date of M dwarfs ranging from $7 < M_r < 16$ in the optical ugriz system (Fukugita et al. 1996). Results from the work presented by this paper use Bessell R- and I-bands (1979, 1990) for photometric parallax relations for $11 < M_R < 14$.

2. Methodology

2.1 Observations

Data were collected over the course of 8 nights between October 2010 and October 2011 with SARA-North's 0.9 m telescope. All observations were photometric and obtained using the 2048^2 Apogee U42 CCD camera at the Cassegrain focus. This gives a plate scale of 0.8" per pixel when binned 2x2. The telescope is located at Kitt Peak National Observatory near Tucson, AZ.

Program stars, the stars of interest for this research, were picked for observation if they matched specific guidelines. First, they must have distances given by the YTP with errors less than 15%. Also, because the stars selected will have new photometry obtained for this research, they must have no R- and I-band photometry associated with them. In order to make sure they are late-type dwarfs, the search was limited to stars with $B-V > 1.2$ and $M_V > 5$.

All stars were observed in Bessell R- and I-band filters (1979, 1990) and calibrated to the Kron-Cousins standardized system. Photometry obtained using the L filter was placed on the standard system described by Spengler et al. (2012). The wavelengths associated with these filters were listed in Table 1 above.

Standard stars, or stars with well-known photometry, from Landolt (1983, 1992) with added L data from Robertson (private communication, 2011), were observed throughout each night. Care was taken to include red standard stars and a wide range of airmass values. These stars aid the transformation of instrumental magnitudes to standardized magnitudes allowing observations to be compared to others on the same system. This is explained in detail in the next section.

2.2 Photometric Calibrations

Each observation night brings sources of error with it. For example, since CCDs work by utilizing the photoelectric effect, there is thermal noise present in the device. This noise results when temperatures above absolute zero cause electrons to be spontaneously emitted, as if the chip was struck by a photon. The CCD at Kitt Peak is thermoelectrically cooled to roughly -20ºC and remains relatively constant throughout the night thus reducing these stray electrons. Additionally, effects in the CCD, filters, and overall optical path are present and need to be corrected. Calibration data were taken at twilight to account for bias, illumination effects, and the other issues outlined below. The image frames were then processed with the calibration frames using the *imred* and *ccdred* packages in the Image Reduction and Analysis Facility (IRAF) software package.

Flat-field images remove pixel to pixel quantum efficiency variations and illumination variations across the chip such as vignetting or by diffraction caused by dust particles that exist on each filter or due to other problems in the general optical path. This filter dependence requires a flat-field for each filter used. All flat-field frames are of the sky at twilight such that the CCD is uniformly illuminated. The intermediate-band filter

allows fewer photons to reach the CCD and is therefore exposed first during the evening observation run. Each frame is exposed for 5 or more seconds to eliminate any shutter effects. Each pixel on a CCD is a separate detector that has an associated gain, the average number of electrons produced per photon. By exposing the CCD to a uniform flux, one can adjust the gains so response is uniform by balancing out this gain.

There exists an added pedestal level (or bias) that ensures the input to the analog-digital converter is always a positive value. To find this, bias frames are taken with zero second exposures (or as close to zero as it can get) with the shutter closed. There are many sources of errors that result from the electronics that create this bias or external ones like read noise (the ability to correctly read out a pixel). To reduce the effects of noise, we combine 20 bias frames into a master bias frame.

Dark frames identify any current that is still present even after the CCD is thermoelectrically cooled to reduce the thermal energy of the atoms and therefore this effect. Four dark frames are exposed for two-hundred seconds in order to obtain good statistics on each pixel without saturating it. This procedure is done last, after sunset, in order to have the darkest possible conditions in case there are any light leaks in the system.

After the above calibration frames are applied to object frames using IRAF, an image frame containing the flux from the sky and stars in the field remains. The IRAF packages *digiphot* and *daophot* through the *daofind* and *phot* tasks were used to measure aperture photometry with an aperture roughly 3 to 4 times the full width half max of the star images. The aperture used was 12 pixels in diameter. The *daofind* task is used first to get information on stars in the field that are the brightest. This saves time as one does not

need to find each star individually in the frame. After the identification or tagging of the brighter stars, program stars that were too faint to be selected by *daofind* need to be identified individually using the *phot* task. It is essential that every program and standard star be identified correctly in all filters in order to obtain correct photometry for each pass-band.

Once this step is completed, an instrumental magnitude for each filter is found with the following equation:

$$v = -2.5 \log\left(\frac{N_V}{t}\right) \qquad 2.1$$

where N_v/t is the total number of counts (ADU's) measured in t seconds. The resulting instrumental magnitude then needs to be put onto a standardized system, a process explained in detail in the next section.

2.3 Photometric Consistency

Standard star observations are taken roughly every hour throughout the night. The photometry collected for these stars allow one to transform instrumental magnitudes to standardized magnitudes. The model used to do this for the V magnitude is as follows:

$$v = V + v_1 + v_2 X + v_3(R - I) + v_4 X(R - I) + v_5(R - I)^2 \qquad 2.2$$

where v is the instrumental magnitude and V is the apparent magnitude on the standard system. The coefficient v_1 is the zeroing term that depends on the observing night. Equation 2.2 can be put into the form of a least-square problem where v-V is the dependent variable and where the fitting parameters are the v_n coefficients. The independent variables are those that contain one of the following: the airmass term, X, and the color index on the standard system, R-I. These independent variables and the instrumental magnitude come from each frame individually.

The airmass coefficient (v_2), known as the linear extinction term, is used to correct for absorption or scatter of the source's light through the Earth's atmosphere. In addition, airmass multiplied by the color term (v_4) corrects for how the atmosphere alters the magnitude for stars emitting in different wavelengths. In order to get good statistical extinction terms, one needs to observe standard stars with a large range of airmass values and color.

The color terms (v_3, v_5) allow for the transformation between filter systems that have different effective wavelengths. The second-order color term corrects for the large range in colors seen in standard stars and for the differences in effective wavelength for the standard system based on photomultiplier tube observations by Bessell (1979, 1990) and the CCD system used in this study.

In order to solve for the zero point fitting parameter for each night, the *fitparams* task in IRAF is used for each night independently. With *fitparams*, one can look at all the standard instrumental magnitudes taken over a night, compared to those given in Landolt (1983, 1992) and delete any with large residuals. With *fitparams*, one can also solve for the other fitting parameters needed to complete the transformation equations.

Even though the *fitparams* task gives adequate transformation equations, it may be useful to take into account all observation data when finding the transformation coefficients. The more information about the observing conditions and instrumentation, the more accurate the transformation will be. Transformation coefficients found using multiple nights were used to put all instrumental magnitudes obtained for this research onto a standard system. In order to obtain the best possible transformation coefficients, all standard star observations for the first 7 nights were included in a multivariate model to determine values for the fitting parameters 2-5 for each color. These resulting fitting parameters, listed in Table 2, were used for all 8 nights. Zero point parameters were still determined for each night using *fitparams*, however, giving a final transformation equation. Standardized magnitudes can then be obtained with the *invertfit* task.

TABLE 2
Fitting Parameters for Transformation Equations

	V	R	I	L
v_2	0.163 ± 0.008	0.115 ± 0.008	0.045 ± 0.011	0.098 ± 0.010
v_3	0.036 ± 0.022	0.039 ± 0.023	-0.094 ± 0.031	0.028 ± 0.017
v_4	0.024 ± 0.015	0.024 ± 0.016	0.041 ± 0.021	-
v_5	-0.019 ± 0.005	0.029 ± 0.006	-0.038 ± 0.007	0.047 ± 0.010

3. Data Reduction

3.1 Binary Systems and Interstellar Reddening

The YTP catalog includes data on stars, even if they exist in known binary systems. It is important to exclude these binaries from the observing list and analysis, as their apparent magnitudes will be affected by the presence of a companion. There also exist close companions (optical doubles) to some of the program stars that can give inaccurate flux measurements when processing in IRAF. These stars are found while analyzing data and subsequently removed.

When observing in pass-bands close to the near-infrared, interstellar reddening due to dust obstruction is minimized. Extinction mainly affects short wavelength observations close to the Galactic plane. Since all observations are in longer wavelengths, and especially since all program stars are close to the Sun, there is no need to correct for this extinction.

3.2 Lutz-Kelker Corrections

Absolute magnitudes calculated using distances from trigonometric parallaxes have an inherent systematic bias associated with them. This bias affects the accuracy of photometric parallaxes if it is not removed. This results from the inverse relationship

between a star's parallax angle and distance. Since the two are inversely proportional, there are asymmetric errors. This leads to distance being on average underestimated (parallax angle is then overestimated). This in turn underestimates the star's luminosity. However, corrections can be made since it is directly related to the accuracy of the parallax angle (Lutz & Kelker 1973).

This correction of this bias is explained in detail by Hanson (1979), but has been simplified here. Corrections to absolute magnitude values can be calculated with the following relation:

$$\Delta M_{LK} = -2.17\left(\left(n+\frac{1}{2}\right)\left(\frac{\sigma_p}{p}\right)^2 + \left(\frac{6n^2+10n+2}{4}\right)\left(\frac{\sigma_p}{p}\right)^4\right) \qquad 3.1$$

where n is found using the cumulative proper motion distribution, $N(\mu)$, where μ is proper motion and p is the parallax angle in arcseconds. $N(\mu)$, represented by a power law, μ^{-n}, is plotted against μ in Figure 2. The resulting fit gives us an n-value approximately equal to 2, which will be used in Equation 3.1. The n = 2 and n =3 cases for systematic magnitude corrections are plotted in Figure 3 against relative error for our stars. These curves match the ones given in Hanson's paper.

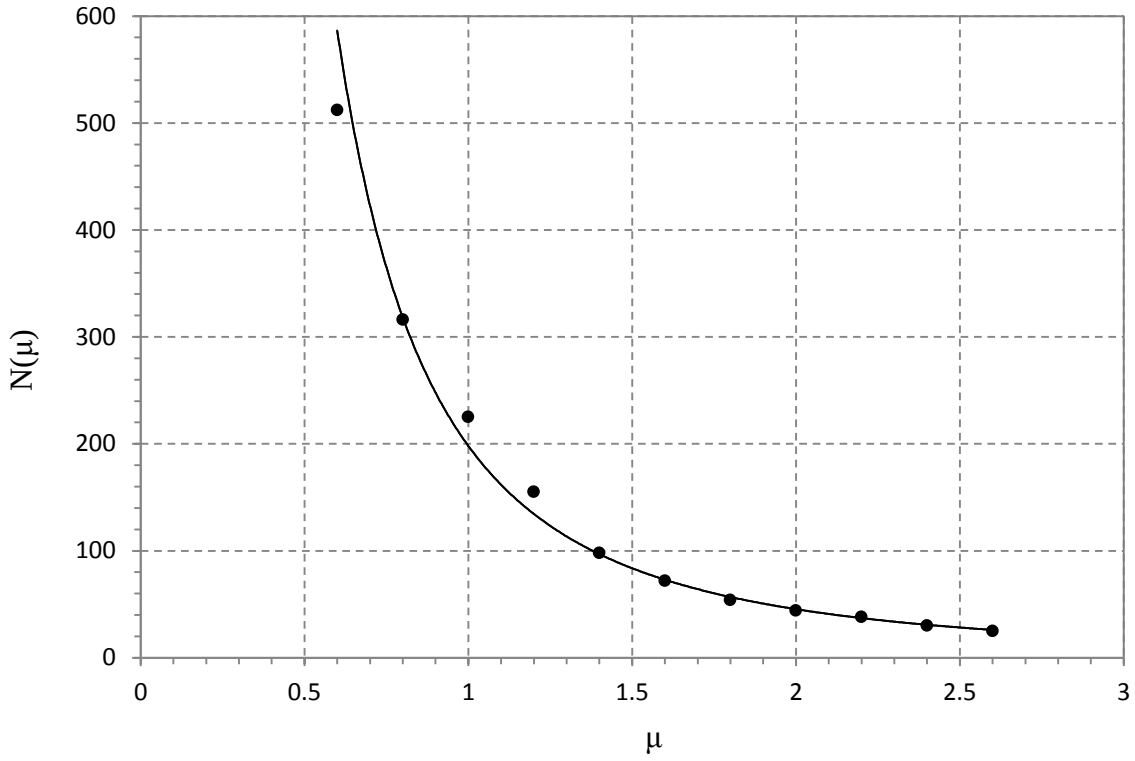

Fig. 2.- Parallax Star Proper Motion Distribution - Proper motion distribution for 1,242 stars with $\mu > .5''$/yr from the YTP Catalog where N(μ) is the number of stars having proper motions greater than μ. The equation for the fit given is, $N(\mu) = 198.07\ \mu^{-2.125}$, giving $n \sim 2$.

Once an n-value is determined, one can use Equation 3.1 to determine the Lutz-Kelker correction associated with each calculated absolute magnitude that is used for analysis (in this case, M_R). A polynomial fit that represents this corrected data (shown later in Section 4.3) can be found using the corrected magnitudes. One, however, cannot keep this correction for individual magnitudes, but only to represent a sample (Reid & Hawley 2005). Studies that use parallax angles with low uncertainty find the correction is negligible and do not correct for this. However, for a parallax uncertainty of 10% there is a correction of -0.06 mag and for uncertainty of 13% there is a rise in correction to -0.1

mag. The relative parallax errors for this study range from 0.35% to 15% while the mean is 7.6%; therefore, it is necessary to make these corrections.

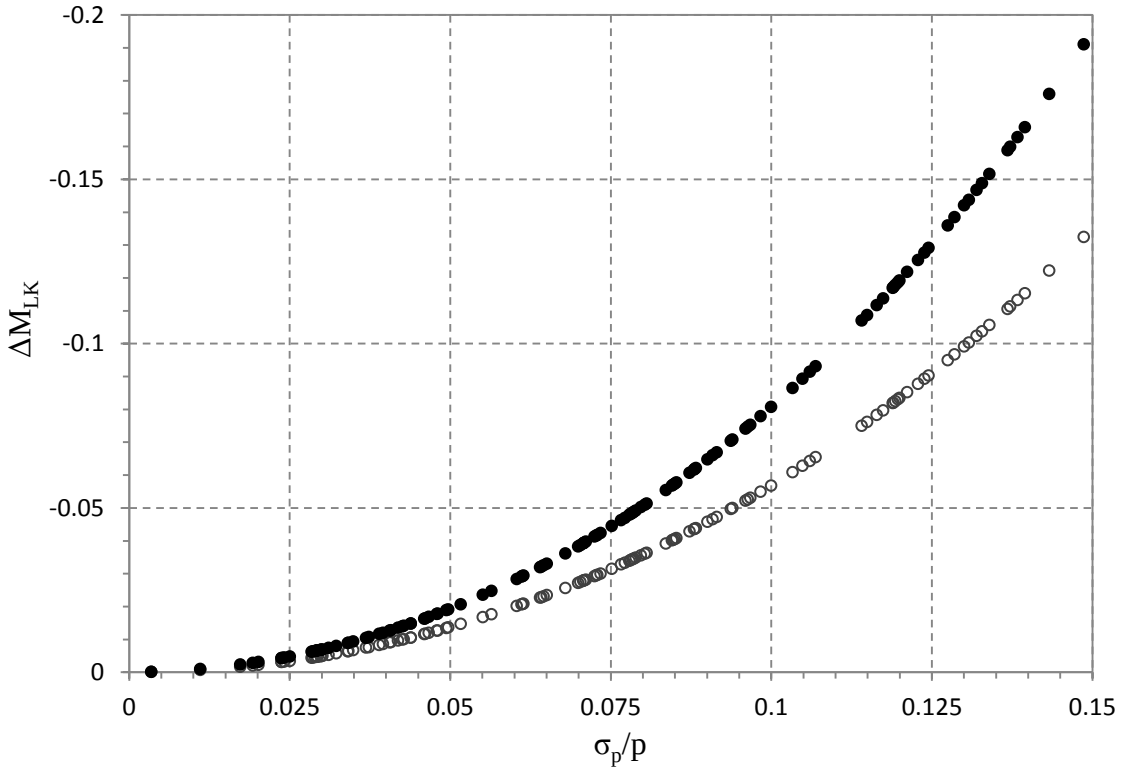

Fig. 3.- Lutz-Kelker Corrections - Lutz-Kelker corrections for Hanson's approximations for a power-law proper motion distribution, $N(\mu) \propto \mu^{-n}$, using program stars from YTP. The case where $n = 2$ is plotted as open circles, and the $n = 3$ case are closed circles.

3.3 Flare and BY Draconis Variable Stars

Out of our 118 observed program stars, 13 are known to be magnetically active, exhibiting short-term luminosity variations. There exists a specific type of variable star, BY Draconis stars, that make up 3 of our 13. The variations in their luminosities are mainly caused by starspots. Therefore, some exhibit cyclic behavior from the rotation of the star. Older stars show a smoother cyclical behavior as their rotation has slowed with

age. Conversely, young stars rarely exhibit this due to their rapid rotation (Pettersen et al. 1992). Research on BY Draconis variables show that they are typically found in binary systems (Bopp & Fekel 1977); however, the 3 in our sample have no detected companion. Their place on the CMD does not indicate any systematic bias and therefore they are included in the analysis.

In addition to starspots, stellar flares can brighten the star by 2.6 magnitudes over the course of only seconds to minutes (Luyten 1949). These random flares are therefore easy to identify while observing. As a result, they do not pose a problem as all 10 flare stars lie close to the disk main sequence.

4 Data Analysis

4.1 Error Analysis

Throughout the process of changing instrumental magnitudes to standardized ones, care was taken to minimize the residuals between standard star observations for this work and those given by Landolt (1983, 1992) and Robertson (private communication, 2011). Residuals between the two are plotted in Figure 4 below for each calculated pass-band and color index. Figure 1.a – 1.c show no systematic trends that would affect the magnitude values. However, in Figure 1.d, there is evidence of systematic bias for redder stars. Our standard star observations consist of mainly warm standards, stars with R-I < 0.7. The program stars have R-I values greater than this, and yet only about 10 of the 109 standard star observations are in that range. Since transformation equations have terms that rely on color, it is important to increase the number of red standards observed in the future.

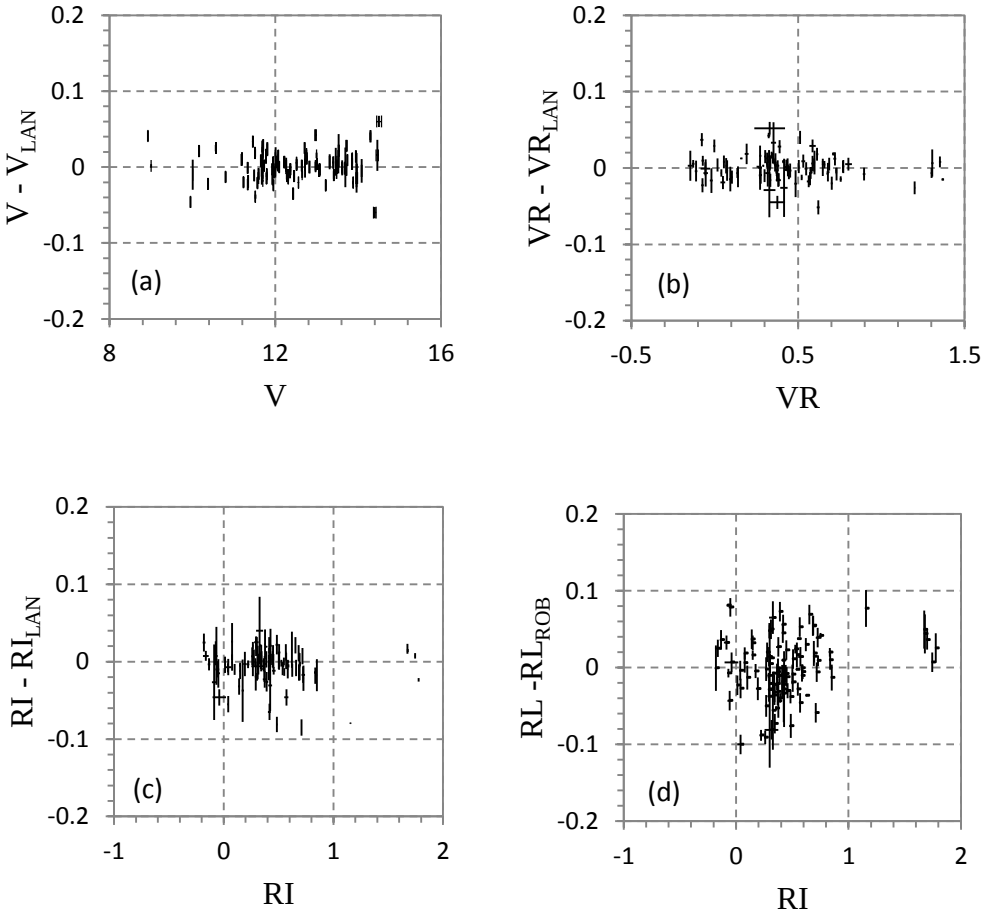

Fig. 4.- Photometric Consistency - Magnitude and color differences between our standard observations and for (a) through (c) Landolt's (1983, 1992). Plot (d) uses Robertson's (private communication, 2011) L-band photometry.

Although the reductions discussed above in Section 2.2 minimize noise in a frame, a certain amount of error is still present in each instrumental magnitude. Of the 118 program stars observed over 8 nights, 44 were observed on multiple nights. With these multiple observations, one can find the degree to which the data are reproducible. To find this, the standard deviation between two or more independent magnitudes was

calculated. The average of these deviations was used as the uncertainty for single observations for (R-I), (R-L) color, and R magnitudes.

Additionally, 2 exposures of the same object were taken back-to-back while observing. The standard deviation between these multiple observations gives a sense of what statistical uncertainty arises from the exposure times being used. This in turn gives a limit on the error. The broadband photometry averaged an error of ±0.01 mag while the intermediate-band averaged ±0.02 mag.

Our broadband color, R-I, has an associated error ranging from ±0.001 to ±0.040 mag with a mean of 0.011 mag. Whereas our intermediate-band color, R-L, error ranges from ±0.001 to ±0.085 mag with a mean of 0.017 mag. This error is larger than the broadband color's error due to poorer statistics in L observations, considered acceptable in the original application of the system. For R magnitudes, errors range from ±0.003 to ±0.083 mag with a mean of 0.024 mag (Bevington 2003).

4.2 Photometric Parallaxes

A main application of a CMD, (M_R, (R-I)) in this case, is to estimate photometric parallaxes. One advantage of observing in the R- and I-bands is that both are observable with the same CCD device, which also has higher quantum efficiency for longer wavelengths (Reid & Hawley 2005). The flux observed using R and I pass-bands is also much greater than when observing with B and V for red dwarf stars, giving one shorter exposure times. In addition, extensive standard star observations exist for R and I pass-bands making the standardized magnitudes well defined. All aid in obtaining more accurate photometric parallaxes.

As explained above in Section 1.2, Siegel et al. (2002) published their own (M_R, (R-I)) diagram with associated main sequence polynomials. They found that the disk dwarf main sequence appears to change slope at R-I ~ 1 giving the following two equations:

$$M_R = -6.862 + 61.375(R-I) - 108.875(R-I)^2 + 90.198(R-I)^3 - 27.468(R-I)^4 \quad 4.1$$

$$0.4 \leq R - I < 1.0$$

$$M_R = -114.355 + 408.842(R-I) - 513.008(R-I)^2 + 286.537(R-I)^3 - 59.548(R-I)^4 \quad 4.2$$

$$1.0 \leq R - I < 1.5$$

for late K to early M-type stars. These data and associated fits are plotted in Figure 5.

On this same figure, data for the 118 program stars observed for this paper are plotted as filled shapes. The cooler region of the CMD, R-I ≥ 1.5, contains 63 of the 118 stars. These were used to obtain the following polynomial:

$$M_R = -274.73 + 476.77(R-I) - 265.64(R-I)^2 + 49.715(R-I)^3 \quad 4.3$$

$$1.5 \leq R - I < 2.0$$

which represents late disk M dwarf stars. The graph in Figure 5 will be explained in more detail in Section 5.1.

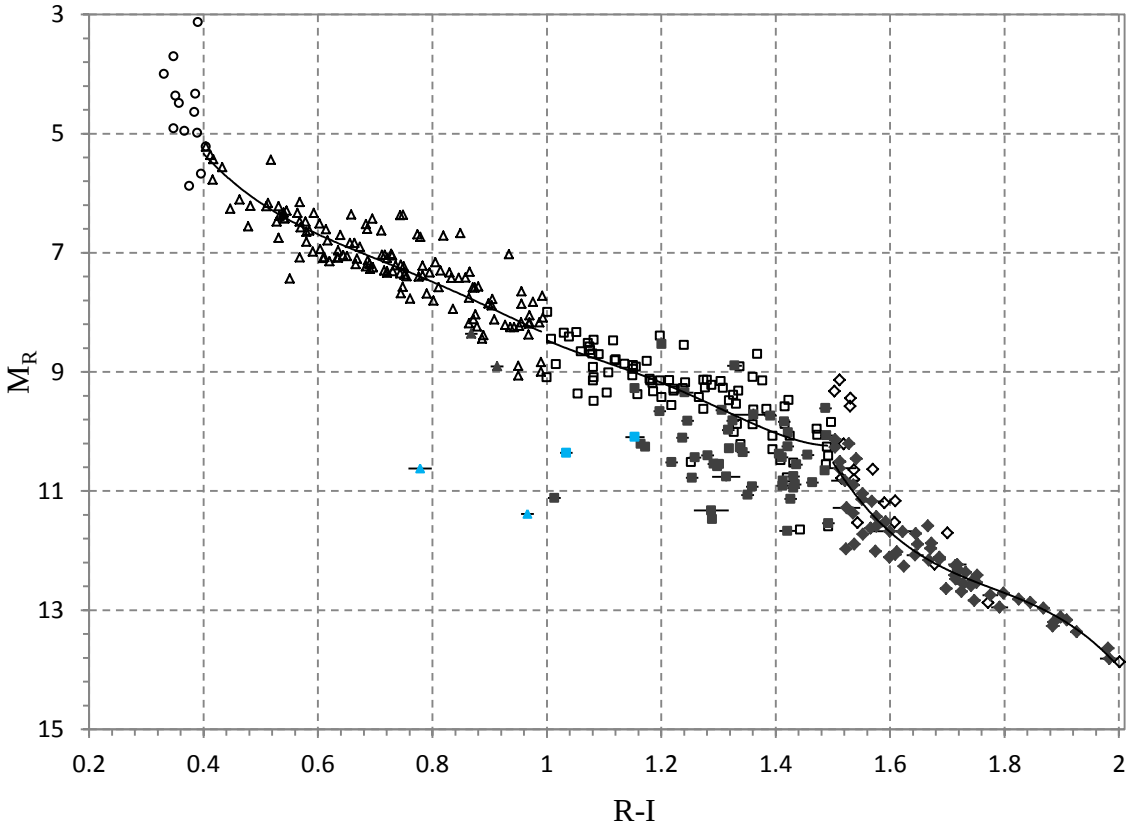

Fig. 5.- (M_R, (R-I)) Color-Magnitude Diagram - CMD plotting Bessell (1990) and Leggett (1992) photometry with distances from *Hipparcos* (open shapes) and our program stars (closed shapes). The open shapes are separated such that circles have R-I < 0.4, triangles have 0.4 ≤ R-I < 1.0, squares have 1.0 ≤ R-I < 1.5, and diamonds have R-I ≥ 1.5. Closed shapes follow the same trend. The solid lines show three different fits to these data with the first two given by Siegel et al. (2002) (Equations 4.1 & 4.2) and the last presented with new observations and YTP distances excluding known binaries (Equation 4.3). Blue data points represent previously published subdwarf stars.

Parallax errors given by YTP strongly affect the precision of calculated absolute magnitudes. In fact, in nearly all cases, parallax errors are much larger than photometric errors. Regardless, both carry over into absolute magnitude error by applying standard error analysis. The errors for M_R (ones used to obtain Equation 4.3) range from ±0.01 to ±0.10 mag with an average of ±0.04 mag. The average scatter for this new curve fit is ±0.30 mag in M_R for 1.5 ≤ R-I < 1.7 and ±0.10 mag for 1.7 ≤ R-I < 2.0. With Equation

1.2, the average errors, and average scatter stated above, one can find an approximate error for a distance calculated using Equation 4.3. For $1.5 \leq$ R-I < 1.7, the average error is about 14%, and for $1.7 \leq$ R-I < 2.0, the average error is about 5%. The average error for distances given by YTP in our sample is about 8%. The error propagation used is the same as described by Bevington (2003).

4.3 Two-Color Diagram

It is desirable to observe in as few pass-bands as possible while still obtaining vital information on stars of interest. TCDs can offer a tight trend that allows for the calculation of an unknown color. For instance, ((V-I), (R-I)) is plotted in Figure 6. This curve is represented by the following:

$$V - I = -0.3746 + 3.789(R - I) - 2.039(R - I)^2 + 0.5711(R - I)^3 \qquad 4.4$$

$$0.3 \leq R - I \leq 2.01$$

which excludes possible and known subdwarf stars. The average scatter in $V - I$ is 0.02 mag for this curve fit.

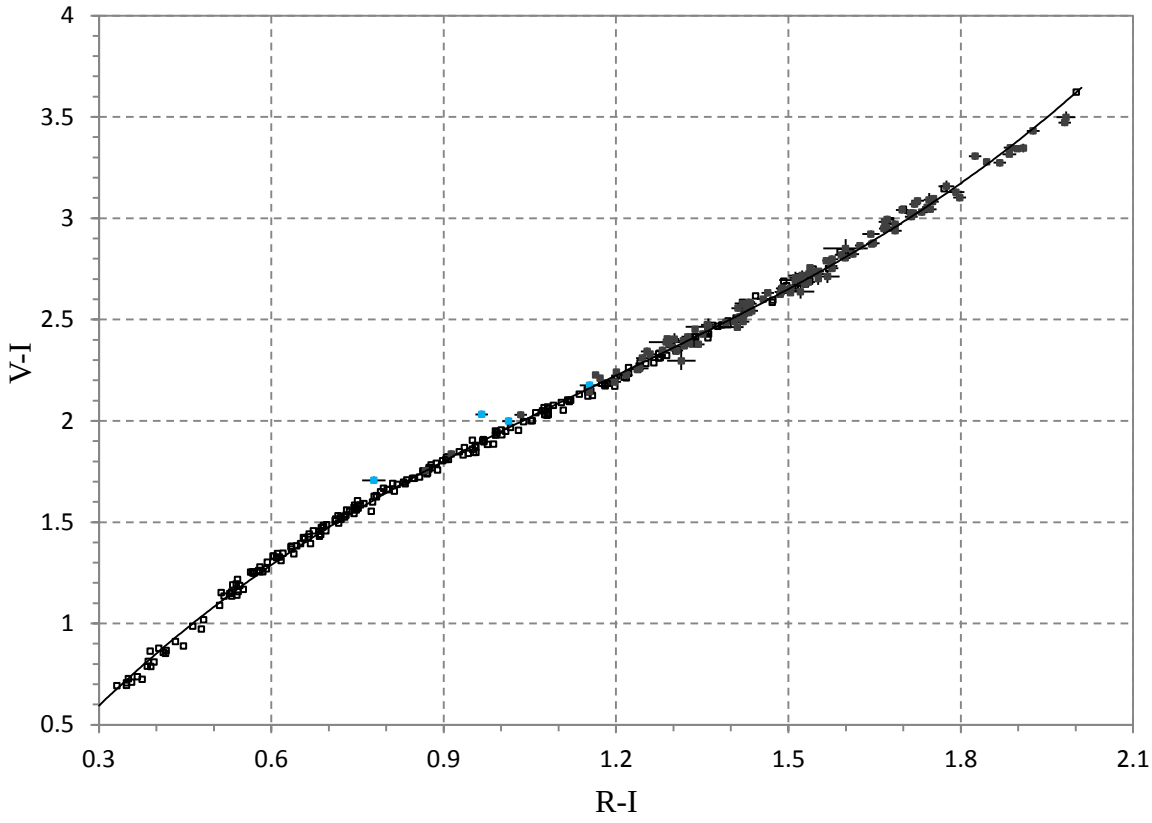

Fig. 6.- ((V-I), (R-I)) Two-Color Diagram - TCD showing the relation between R-I and V-I excluding known binaries. Previously published subdwarfs are in blue. Bessell (1990) and Leggett (1992) data are plotted using open squares while the data obtained for this research are filled squares.

TCDs also aid in the discrimination of low metallicity stars. Figure 7 shows ((V-R), (R-I)) where the separation between the disk dwarfs and subdwarfs is more apparent. This separation mainly reflects the fact that subdwarfs are bluer in *R-I*. Since subdwarfs lie about 0.1 magnitudes above the curve, and error for color indexes can be as high as ±0.04 mag, broadband photometry is not a reliable discriminator for disk/halo stars (Reid & Hawley 2005). The next section describes in detail on detection methods for subdwarf stars using intermediate band photometry.

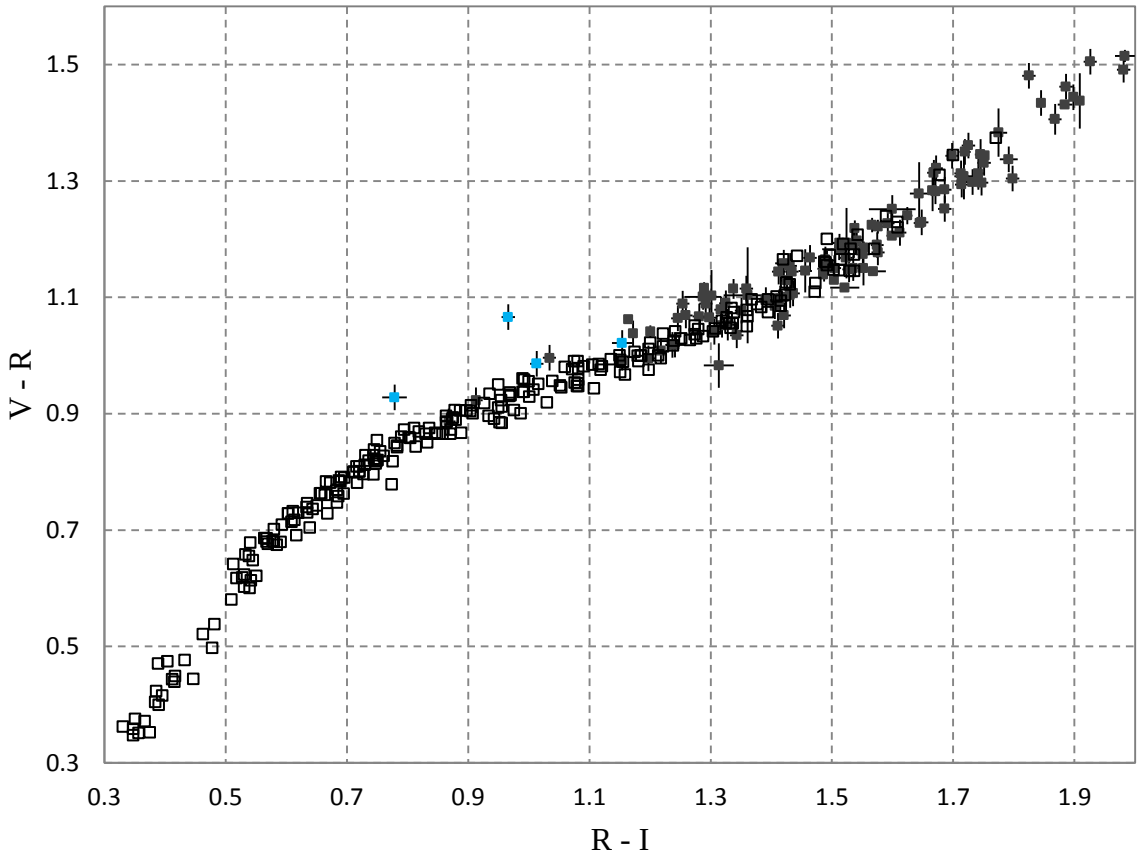

Fig. 7.- ((V-R), (R-I)) Two-Color Plot - TCD for disk dwarf stars observed (filled squares) and photometry from Bessell (1990) and Leggett (1992) (open squares) with published subdwarfs (blue points) lying above the disk main sequence.

4.4 Subdwarf Identification

As all observed stars lie relatively close to the curve in the color range R-I > 1.5 in Figure 5, one does not expect to see any subdwarf stars for that region. As a result, Equation 4.3 is unaffected. However, for late K to early M-type stars having R-I < 1.5, there appears to be some scatter indicating subdwarf stars in that range. Photometric parallax estimates on average underestimate luminosities (overestimating distance) for

disk dwarfs due to the presence of these subdwarf stars; removing them is an important part of determining photometric parallaxes in Equations 4.1 & 4.2.

Plotted in Figure 8, ((R-L), (R-I)) gives a means to discriminate between M subdwarfs and M disk dwarf stars. Stars in this figure are plotted by groups based on difference in absolute red magnitude, ΔM_R, in standardized deviation units from Siegel's curves (Equations 4.1 & 4.2) and the one presented by this research (Equation 4.3). To calculate these values, an absolute red magnitude is calculated from one of the equations and then subtracted from its actual value (obtained using YTP distances) to get ΔM_R for each set of R-I values. The standard deviation was calculated for each set to get $\Delta M_R/\sigma$. ($\Delta M_R/\sigma$, (R-I)) is plotted in Appendix A.1 for reference. These values were used to separate the stars into the groups seen in the Figure 8. This allows one to see the position of the star on the CMD while looking at the ((R-L), (R-I)) TCD.

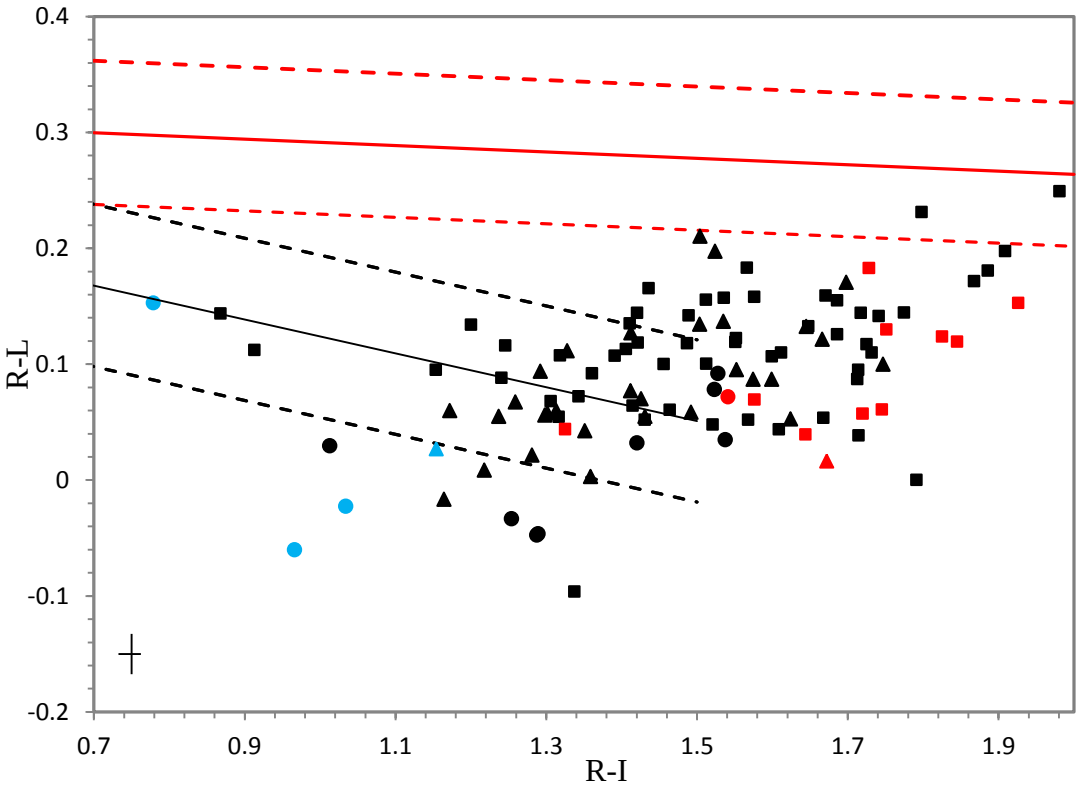

Fig. 8.- ((R-L), (R-I)) Two-Color Diagram - Squares are in the range $0.0 \leq \Delta M_R/\sigma < 1.0$, triangles $1.0 \leq \Delta M_R/\sigma < 2.0$, circles $2.0 \leq \Delta M_R/\sigma < 4.0$, blue symbols are known subdwarfs, and red symbols are known flare stars. The typical error for all data is located in the lower left corner of the graph. The disk dwarf population is displayed as a solid black line with the dashed black lines lie at ±2σ from this population. Known giant stars are represented by the red solid line with ±2σ marked with dashed red lines (Humphrey & Robertson 2008).

The disk dwarf population is portrayed by the solid black line with the dashed lines at ±2σ. Generally, stars that lie outside these lines require explanation. The circles in Figure 8 are stars that lie farthest below the (M_R, (R-I)) curve (Fig. 5) ranging from $2.0 \leq \Delta M_R/\sigma < 4.0$, triangles have $1.0 \leq \Delta M_R/\sigma < 2.0$, and squares $0.0 \leq \Delta M_R/\sigma < 1.0$. The majority of stars below -2σ from the disk dwarf sequence have larger $\Delta M_R/\sigma$ indicating subdwarf qualities. Their position in Figure 8 indicates both larger effective temperature and stronger CaH absorption. These stars will be discussed more in Section 5.2.

5. Results and Discussion

5.1 Photometric Parallax

The updated (M_R, (R-I)) CMD, Figure 9, has been expanded to include later M-type stars using distance estimations from YTP and photometry obtained with the SARA 0.9 m telescope. Appendix A.2 lists all magnitudes put on the standard system with associated $\Delta M_R/\sigma$ from each curve fit (given by Equations 4.1 - 4.3). All fits were corrected for Lutz-Kelker bias, although this has not been applied to individual magnitude values.

The almost vertical trend at R-I ~ 1.5 can be explained as it does not account for earlier stars. Similarly, Siegel's polynomial for $1.0 \leq$ R-I < 1.5 has a shallow slope at R-I ~ 1.4 as it does not include later type stars. Combining both sets of data will account for this. The blue points in our new CMD now represent results presented in the next section.

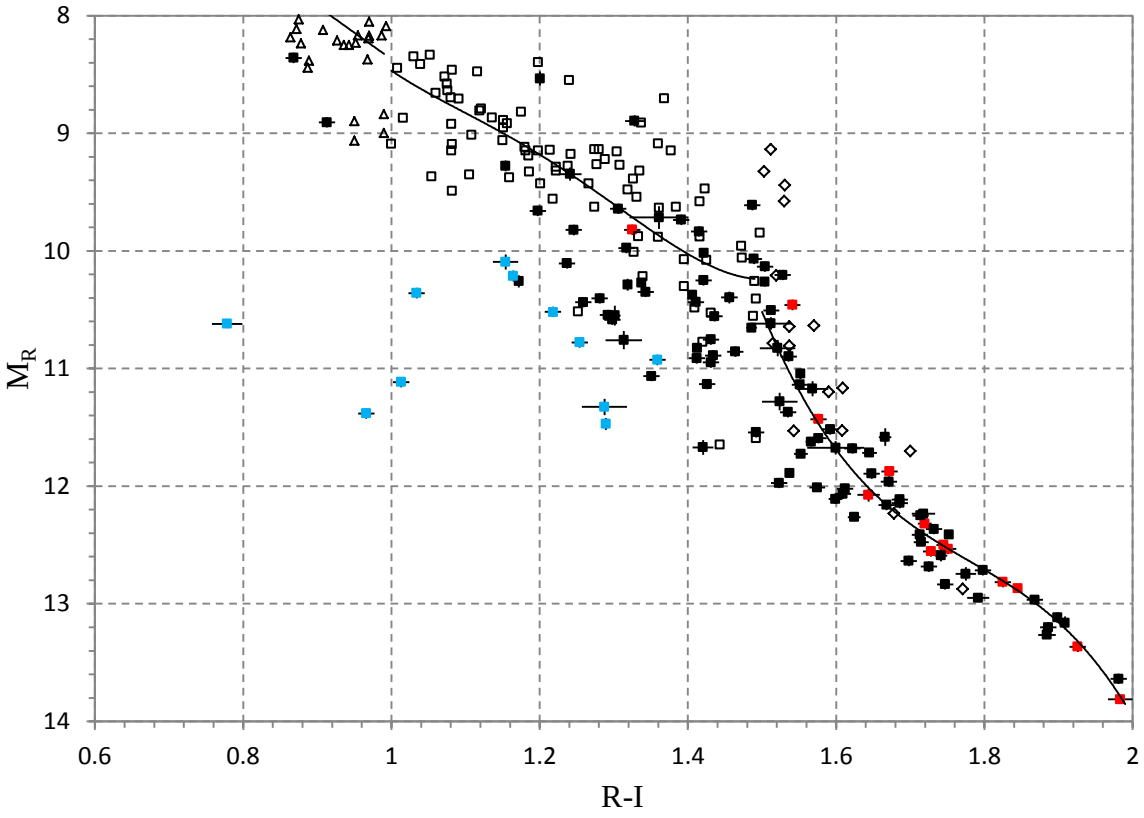

Fig. 9.- (M_R, (R-I)) Color-Magnitude Diagram Identifying Subdwarfs - CMD with subdwarfs identified using ((R-L), (R-I)) plot are plotted in blue. Known flare stars are plotted as red. Our data is plotted with filled squares and open symbols are from Bessell (1990) and Leggett (1992) with distances from *Hipparcos*.

5.2 Subdwarf Main Sequence

As mentioned above, the subdwarf population in our CMD (see Fig. 9) does not appear to affect the curve fit for late M dwarfs, but will affect early M dwarf photometric parallaxes. Figure 8 above plots a ((R-L), (R-I)) TCD as a means to identify these subdwarf stars. There exists a group of stars below -2σ from the disk dwarf main sequence discussed above. Of these 11 stars, 10 of them also lie below the disk main sequence on the CMD. These are listed in Table 3 and plotted in blue in Figure 10. Their position on this TCD, in addition to their placement on the CMD, indicates strong CaH absorption and therefore low

metallicity (Jao et al. 2008). In fact, 3 of these stars have been previously classified as subdwarf (sd) or extreme subdwarf (esd) stars by Gizis (1997) or type VI, a subdwarf classification used by Jao, W. et al. (2008).

Object G005-022 was published as esdK7 (Reid & Gizis 2005) using the method developed by Gizis (1997). Although G005-022 lies well below the disk dwarf main sequence with a $\Delta M_R/\sigma$ of 2.28, it lies on the disk main sequence line in the ((R-L), (R-I)) TCD. Although this star has a small error associated with it in (R-L), more data may be needed to give a better representation of the (R-L) value and associated error.

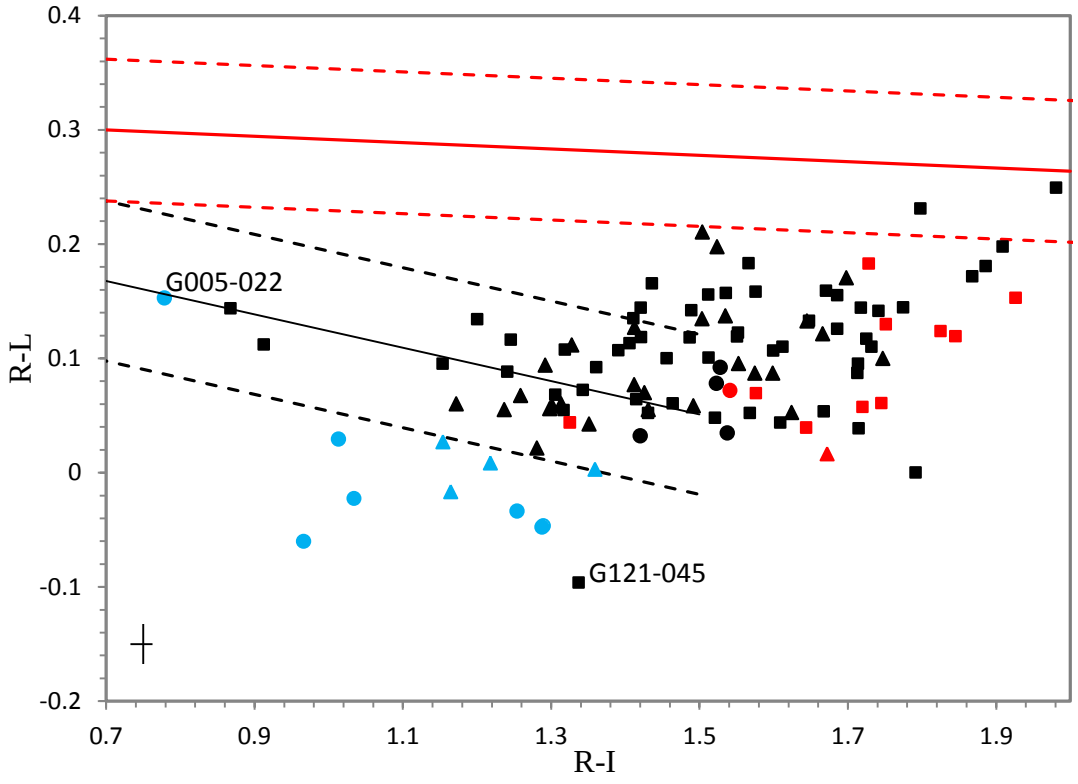

Fig. 10.- ((R-L), (R-I)) Two-Color Diagram Identifying Subdwarfs - TCD with same symbols as in Figure 8 but with subdwarfs identified using the described method plotted in blue.

A single star exists below -2σ from the disk dwarf sequence in ((R-L), (R-I)) yet lies close to the disk dwarf main sequence in the CMD. This star, G121-045, has been previously published as a dwarf star. Given accurate photometry and trigonometric parallax data, G121-045's placement in the TCD may be a result from higher gravity, and therefore stronger CaH absorption, than a typical disk dwarf star. Furthermore, there exists the possibility that its measured parallax, at an error of 8% with 2 parallax observations, is inaccurate therefore affecting G121-045's position on the CMD and $\Delta M_R/\sigma$.

These issues may also be in affect for the stars with large $\Delta M_R/\sigma$, but that are close to the disk main sequence on the TCD. There are 5 of these objects, all with R-I ~ 1.5. As explained in the previous section, each curve fit near this R-I value (Equations 4.2 & 4.3) do not represent the complete data set, which may be the cause for some of the larger $\Delta M_R/\sigma$ values. While combining each data set to find a single polynomial fit will help this issue, there is still a noticeable change in slope that occurs at R-I ~ 1.5 (M4-type). Reid and Cruz (2002) suggest that this large change in luminosity over a relatively small change in color indicates a significant change in the stellar structure, since it is apparent over a large range of wavelengths. To date, there is no widely accepted theoretical cause for this change in the main sequence but it is theorized that it may be caused by the onset of full convection in M dwarf stars (Reid & Hawley 2005). As such, this method of identifying subdwarf stars appears to be effective for $0.8 < R\text{-}I < 1.4$.

TABLE 3
Possible Subdwarfs

R.A. (J2000) (h:m:s)	Decl. (J2000) (d:m:s)	Object	M_R[1] (mag)		(R-I)[2] (mag)		(R-L)[3] (mag)		Predicted M_R[4] (mag)	$\Delta M_R/\sigma$[5]	Previous Spectral Type[6]
14 47 53.4	-03 09 15	G124-072	10.8	±0.04	1.25	±0.01	-0.03	±0.01	9.40	2.0	M2
10 14 27.6	+43 53 45	L1617-23	10.2	±0.05	1.16	±0.00	-0.02	±0.02	9.05	1.7	-
12 02 30.6	+08 25 10	G011-035	10.1	±0.06	1.15	±0.02	0.03	±0.02	9.01	1.6	sdM2
14 19 09.2	-07 18 55	G124-023	10.9	±0.04	1.36	±0.01	0.00	±0.00	9.86	1.6	M3
04 56 06.7	+25 54 02	G039-041	10.5	±0.05	1.22	±0.01	0.01	±0.03	9.25	1.9	M
14 06 57.7	+38 35 50	G165-047	11.4	±0.04	0.97	±0.01	-0.06	±0.01	8.22	2.2	esdM1.5
11 59 38.2	+62 27 49	G237-038	11.1	±0.04	1.01	±0.01	0.03	±0.02	8.52	3.8	M
02 58 11.6	-12 53 02	L802-6	11.5	±0.05	1.29	±0.01	-0.05	±0.01	9.56	2.8	M2.5
08 02 55.5	+25 34 08	G090-039	11.3	±0.07	1.29	±0.03	-0.05	±0.00	9.55	2.6	M
21 07 46.5	+59 41 13	G231-027	10.4	±0.04	1.03	±0.01	-0.02	±0.04	8.60	2.6	M1VI

[1]M_R values calculated from YTP and Kron-Cousins R.
[2]R-I colors on the Kron-Cousins system.
[3]R-L colors on the Kron-Cousins and Farris et al. (2012).
[4]M_R calculated from Equations 4.1-3.
[5]$\Delta M_R/\sigma$ calculated using Equations 4.1-3 compared the M_R calculated from YTP and Kron-Cousins R.
[6]Previous spectral types given by SIMBAD.

5.3 CaH and TiO Absorption in Late M Dwarfs

There exist ~40 stars in the $1.4 < R\text{-}I < 2.0$ range that lie above $+2\sigma$ from the disk dwarf main sequences in Figure 10, if the disk main sequence is to continue as a linear extension toward higher R-I values. Although this placement may indicate high metallicity (strong TiO absorption) or lower gravities (weak CaH absorption), there does seem to be some systematic bias affecting these observations. This systematic bias is the most likely cause for the stars above $+2\sigma$ in Figure 10, as all stars lie close to the disk main sequence in the (M_R, (R-I)) CMD.

It is interesting, however, to note that 11 of the 13 flare stars (one was excluded due to its large error in R-L) in the sample lie in this R-I range. This may help explain the lack of subdwarf stars in this region, as flare stars are typically younger and therefore have higher metallicities (Sherwood & Plaut 1975). To further support this reason for the lack of subdwarfs, Joy and Abt (1974) observed that later type M dwarfs are generally more active than early types. This activity appears to be a function of age and mass, with lower mass and younger stars retaining their activity for a longer period. A star's activity can be enhanced due its higher rotational rate, observed in younger stars as rotation rate slows with age (Reid & Hawley 2005).

6. Conclusions

The CMD is one of the most useful tools for astronomers. The (M_R, (R-I)) CMD given by Siegel et al. (2002) has been expanded to include 63 late M dwarfs using YTP distances and new photometry. An additional 55 late K to mid M-type stars were added to the existing set. With the updated graph, photometric parallaxes for late M dwarfs were determined. The fits presented in Figure 5 are for three independent sets of data described by Equations 4.1- 4.3. The future goal of this project will be to create a single polynomial fit for late K to late M-type disk dwarf stars ($0.7 \leq R - I$).

A better fit will not only give a more accurate distance determination, but also aid in the identification of subdwarf stars. A star's position on the (M_R, (R-I)) CMD is affected by temperature, metallicity, and gravity. Using this knowledge in conjunction with the TCD, one can effectively identify subdwarf stars. By plotting ((R-L), (R-I)) in groups of $\Delta M_R/\sigma$ found using the fits given by Equations 4.1 - 4.3, 7 previously unknown, sub-luminous stars have been identified. Their position below the disk dwarf main sequence on ((R-L), (R-I)) indicates that these stars have lower metallicity than disk dwarf stars. Given current results, this method of identifying subdwarf stars appears to be effective for $0.8 < R-I < 1.4$.

On the ((R-L), (R-I)) TCD, ~40 objects lie more than +2σ above the disk main sequence. This suggests that these stars have either high metallicities or low gravities. High metallicity in stars is an indication that they are younger than the disk main sequence. It is because of these traits that they fit the profile for younger, less massive, active stars. This may provide a reason for the lack of subdwarf stars in this region, as subdwarfs are older and have lower metallicities than disk or active stars.

However, this does not give a plausible reason as to why close to 40 stars do not follow the disk dwarf trend. As stated above, there is evidence for systematic bias in Figure 1.d. This is most likely due to the lack of red standard stars in catalogs used to obtain transformation coefficients. More observations of red standard stars will need to be obtained and used to acquire better transformation equations with an updated catalog.

Currently, this work presents a more complete CMD that will aid in distance estimations and subdwarf identification. In addition, a new TCD is effective in identifying subdwarf stars for $0.8 < R\text{-}I < 1.4$. With these results, one will be able to obtain more accurate luminosity functions to create a more complete model of our Milky Way. With better spatial distributions one gains the information needed to explain the kinematics and evolution of our galaxy.

Appendix

A.1 ($\Delta M_R/\sigma$, (R-I)) Standardized Differences in M_R vs. R-I

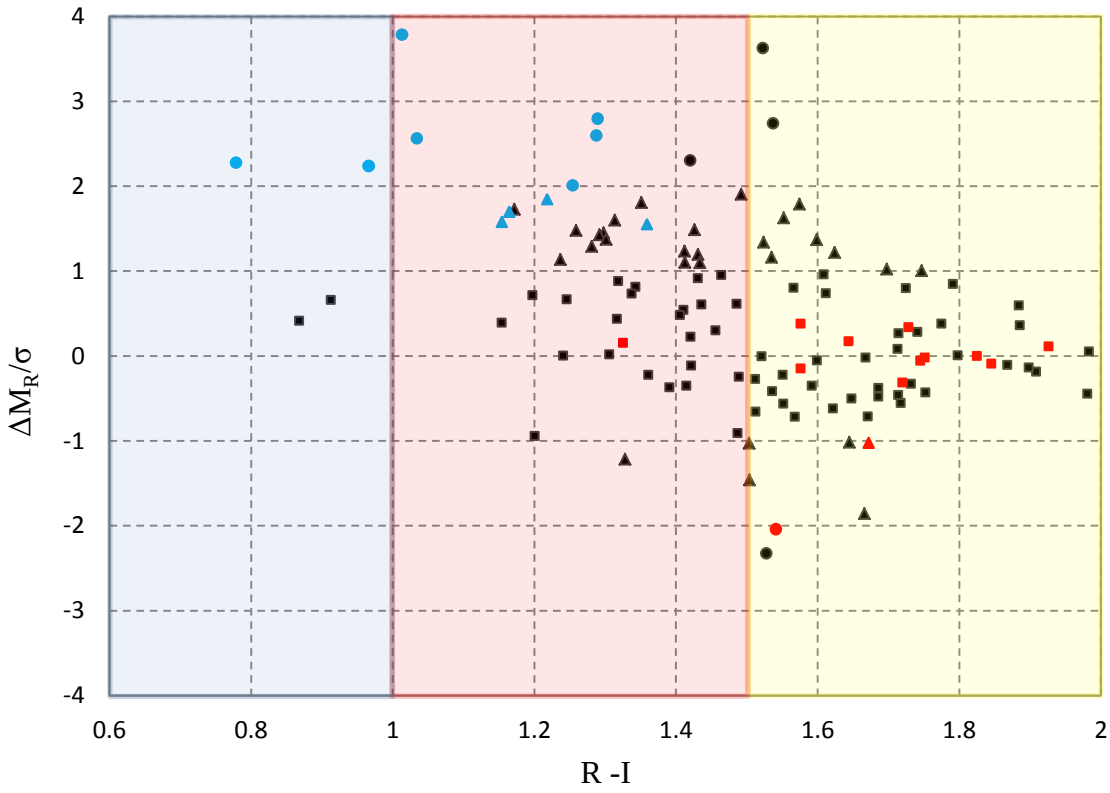

Fig. A.1- Standardized absolute red magnitude differences for values calculated using Equations 4.1 - 4.3 compared M_R calculated from YTP and Kron-Cousins R plotted against R-I. The three colored regions represent the range of R-I for each polynomial: blue for Equation 4.1, red for Equation 4.2, and yellow for Equation 4.3. The shapes and color of each symbol are the same as Figure 8 and Figure 10 - squares are in the range $0.0 \leq \Delta M_R/\sigma < 1.0$, triangles $1.0 \leq \Delta M_R/\sigma < 2.0$, circles $2.0 \leq \Delta M_R/\sigma < 4.0$, blue symbols are known and possible subdwarfs, and red symbols are known flare stars.

A.2 Photometric Data Tables

TABLE A.2
Photometric Data

Name	R^{1}	±	σ_R	$(R-I)^{2}$	±	σ_{R-I}	$(R-L)^{3}$	±	σ_{R-L}	$M_R{}^{4}$	±	σ_{MR}	$\Delta M_R/\sigma^{5}$
G005-022	13.24	±	0.02	0.78	±	0.02	0.15	±	0.01	10.6	±	0.04	2.3
G104-024	11.88	±	0.02	0.87	±	0.01	0.14	±	0.00	8.4	±	0.05	0.4
G015-026	12.50	±	0.02	0.91	±	0.01	0.11	±	0.00	8.9	±	0.05	0.7
G165-047	13.52	±	0.02	0.97	±	0.01	-0.06	±	0.01	11.4	±	0.04	2.2
G237-038	14.36	±	0.02	1.01	±	0.01	0.03	±	0.01	11.1	±	0.07	3.8
G231-027	12.25	±	0.02	1.03	±	0.01	-0.02	±	0.00	10.4	±	0.04	2.6
G011-035	13.04	±	0.02	1.15	±	0.02	0.03	±	0.01	10.1	±	0.05	1.6
G261-046	12.31	±	0.02	1.15	±	0.00	0.10	±	0.02	9.3	±	0.06	0.4
L1617-23	12.63	±	0.01	1.16	±	0.00	-0.02	±	0.02	10.2	±	0.04	1.7
G192-058	11.44	±	0.01	1.17	±	0.00	0.06	±	0.02	10.3	±	0.04	1.7
Ross492	11.59	±	0.02	1.20	±	0.01				9.7	±	0.05	0.7
G170-028	11.37	±	0.01	1.20	±	0.00	0.13	±	0.02	8.5	±	0.05	-0.9
G039-041	13.13	±	0.02	1.22	±	0.01	0.01	±	0.02	10.5	±	0.05	1.8
L1268-3	12.77	±	0.02	1.24	±	0.01	0.06	±	0.01	10.1	±	0.07	1.1
L1608-2	12.10	±	0.02	1.24	±	0.02	0.09	±	0.01	9.3	±	0.05	0.0
G207-022	10.99	±	0.02	1.25	±	0.01	0.12	±	0.00	9.8	±	0.05	0.7
G124-072	12.25	±	0.02	1.25	±	0.01	-0.03	±	0.01	10.8	±	0.02	2.0
Wolf1339	12.84	±	0.02	1.26	±	0.01	0.07	±	0.01	10.4	±	0.05	1.5
G200-059	12.81	±	0.02	1.28	±	0.01	0.02	±	0.02	10.4	±	0.05	1.3
G090-039	14.05	±	0.04	1.29	±	0.03	-0.05	±	0.00	11.3	±	0.02	2.6
L802-6	11.57	±	0.01	1.29	±	0.01	-0.05	±	0.01	11.5	±	0.08	2.8
G168-032	12.24	±	0.02	1.29	±	0.01	0.09	±	0.01	10.5	±	0.06	1.4
G137-026	11.35	±	0.02	1.30	±	0.01	0.06	±	0.02	10.6	±	0.05	1.4
G226-062	13.66	±	0.05	1.30	±	0.01	0.06	±	0.02	10.5	±	0.05	1.4
G150-034	12.65	±	0.02	1.31	±	0.01	0.07	±	0.01	9.6	±	0.05	0.0
G078-011	13.52	±	0.05	1.31	±	0.02	0.06	±	0.00	10.8	±	0.05	1.6
G064-052	11.96	±	0.02	1.32	±	0.01	0.05	±	0.01	10.0	±	0.05	0.4
G119-029	12.87	±	0.03	1.32	±	0.01	0.11	±	0.00	10.3	±	0.05	0.9
G005-032	11.13	±	0.02	1.33	±	0.01	0.04	±	0.04	9.8	±	0.08	0.2
Ross206	11.61	±	0.03	1.33	±	0.01	0.11	±	0.00	8.9	±	0.04	-1.2
G121-045	11.80	±	0.02	1.34	±	0.00	-0.10	±	0.02	10.3	±	0.07	0.7
G009-007	12.07	±	0.02	1.34	±	0.01	0.07	±	0.00	10.3	±	0.05	0.8

TABLE A.2 (*cont.*)

Name	R^1	±	σ_R	$(R-I)^2$	±	σ_{R-I}	$(R-L)^3$	±	σ_{R-L}	$M_R{}^4$	±	σ_{MR}	$\Delta M_R/\sigma^5$
G103-046	13.72	±	0.02	1.35	±	0.01	0.04	±	0.01	11.1	±	0.05	1.8
G124-023	12.35	±	0.02	1.36	±	0.01	0.00	±	0.00	10.9	±	0.03	1.6
G006-042	11.51	±	0.08	1.36	±	0.04	0.09	±	0.01	9.7	±	0.05	-0.2
G214-012	11.51	±	0.02	1.39	±	0.01	0.11	±	0.01	9.7	±	0.05	-0.4
G087-036	12.25	±	0.01	1.41	±	0.00	0.11	±	0.01	10.4	±	0.05	0.5
G013-026	12.11	±	0.02	1.41	±	0.01	0.14	±	0.00	10.4	±	0.05	0.5
G137-074	12.90	±	0.02	1.41	±	0.01	0.08	±	0.07	10.9	±	0.02	1.2
G170-062	11.64	±	0.02	1.41	±	0.00	0.13	±	0.02	10.8	±	0.05	1.1
LP121-41	11.24	±	0.02	1.42	±	0.01	0.06	±	0.01	9.8	±	0.04	-0.4
LTT17467	13.62	±	0.02	1.42	±	0.01	0.03	±	0.04	11.7	±	0.05	2.3
G092-005	12.80	±	0.02	1.42	±	0.01	0.14	±	0.00	10.3	±	0.05	0.2
G106-035	12.13	±	0.00	1.42	±	0.00	0.12	±	0.03	10.0	±	0.01	-0.1
G149-070	12.13	±	0.02	1.43	±	0.01	0.07	±	0.00	11.1	±	0.05	1.5
LP605-37	11.62	±	0.02	1.43	±	0.01	0.06	±	0.02	10.9	±	0.05	1.2
G002-027	11.76	±	0.02	1.43	±	0.01	0.05	±	0.02	10.8	±	0.05	0.9
Ross837	11.16	±	0.02	1.43	±	0.01				10.9	±	0.06	1.1
G136-076	12.41	±	0.02	1.44	±	0.01	0.17	±	0.03	10.6	±	0.05	0.6
G182-034	12.64	±	0.04	1.46	±	0.01	0.10	±	0.04	10.4	±	0.05	0.3
L1289-229	13.81	±	0.02	1.46	±	0.01	0.06	±	0.01	10.9	±	0.05	0.9
LP57-40	12.17	±	0.01	1.49	±	0.01				10.7	±	0.03	0.6
G144-039	12.24	±	0.02	1.49	±	0.01	0.12	±	0.00	9.6	±	0.05	-0.9
G180-009	12.06	±	0.02	1.49	±	0.01	0.14	±	0.01	10.1	±	0.04	-0.2
G194-050	13.02	±	0.02	1.49	±	0.01	0.06	±	0.02	11.5	±	0.05	1.9
G018-001	12.35	±	0.00	1.50	±	0.01	0.13	±	0.00	10.3	±	0.05	-1.0
G119-037	11.94	±	0.02	1.50	±	0.01	0.21	±	0.01	10.1	±	0.04	-1.5
G183-005	12.36	±	0.04	1.51	±	0.03	0.16	±	0.02	10.6	±	0.06	-0.3
G146-035	12.11	±	0.02	1.51	±	0.01	0.10	±	0.02	10.5	±	0.05	-0.7
L1405-41	14.38	±	0.02	1.52	±	0.02	0.05	±	0.02	10.8	±	0.05	0.0
G069-016	13.40	±	0.02	1.52	±	0.01	0.08	±	0.07	12.0	±	0.05	3.6
G006-018	13.76	±	0.06	1.52	±	0.02	0.20	±	0.02	11.3	±	0.03	1.3
G152-031	13.15	±	0.02	1.53	±	0.01	0.09	±	0.01	10.2	±	0.05	-2.3
LP35-219	11.81	±	0.02	1.54	±	0.01	0.14	±	0.00	11.4	±	0.05	1.2
G013-051	12.37	±	0.02	1.54	±	0.01	0.16	±	0.01	10.9	±	0.01	-0.4
G235-055	13.14	±	0.02	1.54	±	0.00	0.03	±	0.02	11.9	±	0.05	2.7
G068-037	12.17	±	0.02	1.54	±	0.01	0.07	±	0.03	10.5	±	0.01	-2.0
G149-081	11.82	±	0.02	1.55	±	0.01	0.12	±	0.03	11.1	±	0.04	-0.2
G199-017	13.04	±	0.04	1.55	±	0.01	0.12	±	0.02	11.0	±	0.02	-0.6
LP127-132	12.34	±	0.01	1.55	±	0.01	0.10	±	0.02	11.7	±	0.05	1.6

TABLE A.2 (*cont.*)

Name	R^1	±	σ_R	$(R-I)^2$	±	σ_{R-I}	$(R-L)^3$	±	σ_{R-L}	$M_R{}^4$	±	σ_{MR}	$\Delta M_R/\sigma^5$
G136-039	13.61	±	0.02	1.57	±	0.01	0.18	±	0.02	11.6	±	0.05	-0.8
G083-022	13.15	±	0.03	1.57	±	0.02	0.05	±	0.02	11.2	±	0.05	0.7
G087-008	12.64	±	0.01	1.57	±	0.01	0.09	±	0.08	12.0	±	0.04	1.8
G071-045	13.85	±	0.02	1.58	±	0.01	0.16	±	0.02	11.6	±	0.05	0.4
G253-006	11.91	±	0.02	1.58	±	0.01	0.07	±	0.01	11.4	±	0.05	-0.1
LP60-100	13.46	±	0.02	1.59	±	0.01				11.5	±	0.05	-0.4
G203-063	13.27	±	0.02	1.60	±	0.01	0.09	±	0.01	12.1	±	0.02	1.4
G192-026	13.42	±	0.03	1.60	±	0.04	0.11	±	0.01	11.7	±	0.05	-0.1
G107-069	12.30	±	0.02	1.61	±	0.01	0.04	±	0.04	12.1	±	0.05	1.0
LTT3080	10.87	±	0.02	1.61	±	0.01	0.11	±	0.00	12.0	±	0.05	0.7
G105-046	12.99	±	0.02	1.62	±	0.01				11.7	±	0.05	-0.6
G104-037	11.88	±	0.02	1.62	±	0.01	0.05	±	0.01	12.3	±	0.05	1.2
G247-015	12.43	±	0.05	1.64	±	0.02	0.04	±	0.01	12.1	±	0.06	0.2
G146-058	11.79	±	0.00	1.65	±	0.01	0.13	±	0.03	11.7	±	0.05	-1.0
G119-036	11.83	±	0.02	1.65	±	0.01	0.13	±	0.00	11.9	±	0.05	-0.5
LP742-5	14.10	±	0.04	1.67	±	0.01	0.12	±	0.00	11.6	±	0.05	-1.9
G259-015	12.91	±	0.02	1.67	±	0.01	0.05	±	0.01	12.2	±	0.05	0.0
G025-008	12.68	±	0.02	1.67	±	0.01	0.16	±	0.00	12.0	±	0.05	-0.7
G075-030	13.85	±	0.02	1.67	±	0.01	0.02	±	0.06	11.9	±	0.05	-1.0
G136-103	12.46	±	0.02	1.69	±	0.01	0.13	±	0.01	12.1	±	0.03	-0.5
G151-034	13.00	±	0.02	1.69	±	0.01	0.16	±	0.02	12.1	±	0.05	-0.4
G149-094	13.45	±	0.02	1.70	±	0.01	0.17	±	0.00	12.6	±	0.05	1.0
G122-049	11.98	±	0.02	1.71	±	0.01	0.09	±	0.03	12.4	±	0.05	0.1
L788-37	12.34	±	0.02	1.71	±	0.01	0.10	±	0.01	12.2	±	0.02	-0.5
G049-020	12.99	±	0.01	1.71	±	0.01	0.04	±	0.02	12.5	±	0.05	0.3
G112-050	11.95	±	0.01	1.72	±	0.02	0.14	±	0.01	12.2	±	0.05	-0.6
G087-032	13.19	±	0.01	1.72	±	0.01	0.06	±	0.00	12.3	±	0.10	-0.3
LP274-24	14.59	±	0.02	1.73	±	0.01	0.12	±	0.00	12.7	±	0.05	0.8
G085-069	14.15	±	0.02	1.73	±	0.01	0.18	±	0.01	12.6	±	0.06	0.3
G177-052	14.13	±	0.02	1.73	±	0.01	0.11	±	0.00	12.4	±	0.06	-0.3
G039-009	13.95	±	0.03	1.74	±	0.01	0.14	±	0.01	12.6	±	0.05	0.3
Ross594	12.59	±	0.01	1.75	±	0.01	0.06	±	0.01	12.5	±	0.05	-0.1
G260-001	14.19	±	0.02	1.75	±	0.01	0.10	±	0.04	12.8	±	0.05	1.0
G060-055	12.08	±	0.02	1.75	±	0.01	0.13	±	0.07	12.5	±	0.04	0.0
G050-006	13.43	±	0.01	1.75	±	0.00				12.4	±	0.05	-0.4
G139-021	13.31	±	0.05	1.78	±	0.01	0.14	±	0.06	12.7	±	0.04	0.4
G221-005	13.35	±	0.03	1.79	±	0.01	0.00	±	0.07	13.0	±	0.02	0.8
LP639-1	13.35	±	0.02	1.80	±	0.01	0.23	±	0.01	12.7	±	0.05	0.0

TABLE A.2 (*cont.*)

Name	R^1	±	σ_R	$(R-I)^2$	±	σ_{R-I}	$(R-L)^3$	±	σ_{R-L}	$M_R{}^4$	±	σ_{MR}	$\Delta M_R/\sigma^5$
G012-043	11.03	±	0.02	1.83	±	0.01	0.12	±	0.01	12.8	±	0.06	0.0
G077-031	12.53	±	0.01	1.85	±	0.00	0.12	±	0.00	12.9	±	0.02	-0.1
G032-035	13.95	±	0.03	1.87	±	0.01	0.17	±	0.05	13.0	±	0.03	-0.1
G192-015	13.10	±	0.01	1.88	±	0.01				13.3	±	0.05	0.6
LP149-14	14.63	±	0.02	1.89	±	0.01	0.18	±	0.05	13.2	±	0.05	0.4
G139-029	13.64	±	0.02	1.90	±	0.00				13.1	±	0.05	-0.1
G182-036	13.55	±	0.05	1.91	±	0.00	0.20	±	0.02	13.2	±	0.07	-0.2
Ross248	10.87	±	0.02	1.93	±	0.01	0.15	±	0.01	13.4	±	0.05	0.1
G261-006	13.86	±	0.02	1.98	±	0.01	0.25	±	0.01	13.6	±	0.06	-0.4
G201-027	14.07	±	0.03	1.98	±	0.02				13.8	±	0.05	0.0

[1]Apparent R magnitude on the Kron-Cousins system.
[2]R-I colors on the Kron-Cousins and Farris et al. (2012).
[3]R-L colors on the Kron-Cousins and Farris et al. (2012).
[4]M_R values calculated from YTP and Kron-Cousins R.
[5]Standardized absolute red magnitude differences for values calculated from Equations 4.1-4.3 compared the M_R calculated from YTP and Kron-Cousins R.

References

Bessell, M.S. 1979, A&A, 91, 589-607

Bessell, M.S. 1990, A&A, 83, 357-378

Bevington, P. R. 2003, *Data Reduction and Error Analysis for the Physical sciences* (3rd ed. New York: McGraw-Hill)

Bochanski, J. J., Hawley, S. L., Covey, K. R., et al. 2010, AJ, 139, 2679

Bopp, Bernard W., & Fekel, Francis Jr. 1977, AJ, 82, 490-494

De Boer, K. S., & Seggewiss, W. 2008, *Stars and Stellar Evolution* (EDP Sciences)

Farris, L., Spengler, Chelsea, Robertson, T. 2012, JSARA, 6, 5-8

Fukugita, M., Ichikawa, T., Gunn, J. E., Doi, M., Shimasaku, K., & Schneider, D. P. 1996, AJ, 111, 1748

Gizis, John E. 1997, AJ, 113, 806-822

Hanson, R. B. 1979, MNRAS, 186, 875-896

Humphrey, Nick, & Robertson, T. 2008, A&AS Meeting #212, #11.04; BAAS, 40, 204

Jao, W., et al. 2008, AJ, 136, 840-880

Joy, A. H., Abt, H. A. 1974, ApJ, 252, 239

Landolt, Arlo U. 1983, AJ, 88, 439

Landolt, Arlo U. 1992, AJ, 104, 340

Leggett, S. K. 1992, ApJS, 82, 351

Luyten, W.J. 1949, PASP, 61, 179

Lutz, T.E., & Kelker, D.H. 1973, PASP, 85, 573

Pettersen, B. R., Hawley, S. L., Fisher, G. H. 1992, Solar Physics, 142, 197

Reid, I. Neil, Hawley, Suzanne L., Gizis, John E. 1995, AJ, 110, 1838-1859

Reid, I. Neil, & Cruz, K. L. 2002, AJ, 123, 2806-2821

Reid, I. N., & Gizis, J.E. 2005, VizieR On-line Data Catalog: J/PASP/117/676

Reid, I. Neil, & Hawley, Suzanne L. 2005, *New Light on Dark Stars* (2nd ed. New York: Springer-Verlag)

Robertson, T. H. & Furiak, N. M. 1995, BAAS, 27, 1302

Sherwood, Vicki, & Plaut, L. 1975, *Variable Stars and Stellar Evolution* (Springer Science & Business)

Siegel, M.H., et al. 2002, ApJ, 578, 151-175

Skrutskie, M. F., et al. 2006, AJ, 131, 1163a

Spengler, Chelsea, Farris, L., Robertson, T. 2012, JSARA, 6, 9-13

van Altena, W.F., et al. 1995, VizieR On-line Data Catalog: I/238°

York, D. G., et al. 2000, AJ, 120, 1579